ACSNANO

www.acsnano.org

ARTICLE

Signatures of Coherent Phonon Transport in Ultralow Thermal Conductivity Two-Dimensional Ruddlesden–Popper Phase Perovskites

Alexander D. Christodoulides,* Peijun Guo, Lingyun Dai, Justin M. Hoffman, Xiaotong Li, Xiaobing Zuo, Daniel Rosenmann, Alexandra Brumberg, Mercouri G. Kanatzidis, Richard D. Schaller, and Jonathan A. Malen*

Cite This: https://dx.doi.org/10.1021/acsnano.0c03595

Read Online

ACCESS | Metrics & More | Article Recommendations | Supporting Information

ABSTRACT: An emerging class of methylammonium lead iodide ($MAPbI_3$)-based Ruddlesden–Popper (RP) phase perovskites, $BA_2MA_{n-1}Pb_nI_{3n+1}$ (n = 1–7), exhibit enhanced stability to environmental conditions relative to $MAPbI_3$, yet still degrade at elevated temperatures. We experimentally determine the thermal conductivities of these layered RP phases for n = 1–6, where n defines the number of repeated perovskite octahedra per layer. We measure thermal conductivities of 0.37 ± 0.13/0.12, 0.17 ± 0.08/0.07, 0.21 ± 0.05/0.04, and 0.19 ± 0.04/0.03 W/m·K in thin films of n = 1–4 and 0.08 ± 0.06/0.04, 0.06 ± 0.04/0.03, 0.06 ± 0.03/0.03, and 0.08 ± 0.07/0.04 W/m·K in single crystals of n = 3–6. With the exception of n = 1, these thermal conductivities are lower than the range of 0.34–0.50 W/m·K reported for single-crystal $MAPbI_3$. Reduced-order lattice dynamics modeling suggests that the initially decreasing trend of thermal conductivity in similarly oriented perovskites with increasing n may result from the transport properties of coherent phonons, emergent from the superstructure, that do not scatter at the interfaces of organic butylammonium chains and perovskite octahedra. Reduced group velocity of coherent phonons in n = 3–6, a consequence of band flattening in the phonon dispersion, is primarily responsible for their ultralow thermal conductivities. Similar effects on thermal conductivity have been experimentally demonstrated in deposited superlattices, but never in naturally defined materials such as RP phases. GIWAXS measurements reveal that higher n RP phase thin films are less orientationally controlled and therefore possess apparently elevated thermal conductivities relative to single crystals of the same n.

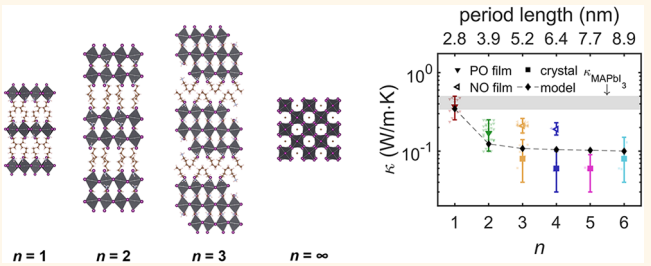

KEYWORDS: *thermal transport, methylammonium lead iodide, 2D perovskites, layered materials, photovoltaics, optoelectronics*

Methylammonium lead iodide ($MAPbI_3$), a hybrid organic–inorganic perovskite (HOIP) belonging to the lead halide perovskite family, is a semiconducting material that has been widely considered for next-generation photovoltaic (PV) and optoelectronic (OE) applications.[1−7] Researchers have exploited its facile processability,[7] notable defect tolerance,[4,6,8] long carrier lifetime,[4,6,9,10] high absorption coefficient,[1] and suitable optical bandgap[2] to develop $MAPbI_3$-based solar cells that have improved in power conversion efficiency (PCE) from less than 3% to 24% in just over a decade.[1,3,11] The impressive external luminescence efficiency and color quality of this HOIP have also made it a material of interest in light-emitting and lasing applications.[1,3,4]

Despite such promising characteristics, $MAPbI_3$ is inherently unstable and tends to rapidly degrade into solid PbI_2 and vaporous MA^+ and I^-.[12,13] This process occurs even in dark vacuum environments and is accelerated by oxygen,[14] moisture,[14−16] light,[15,17,18] and, of central importance to this study, elevated temperature.[15−18] Careful synthesis,[19] encapsu-

Received: April 29, 2020
Accepted: February 19, 2021

ACS Publications © XXXX American Chemical Society

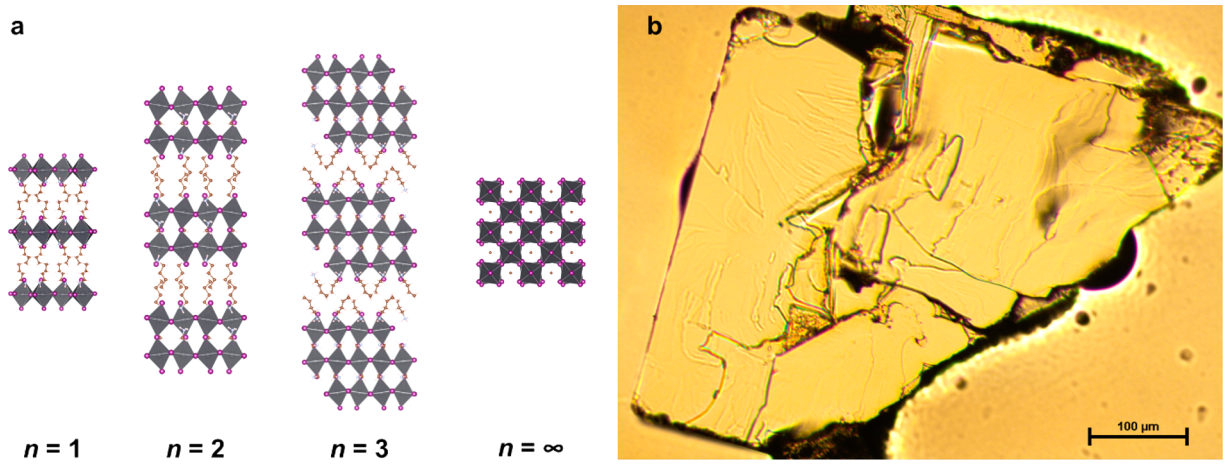

Figure 1. (a) Crystal structure of n = 1−3 homologous members, where n represents the number of perovskite octahedra per organic layer and dictates the thickness of the inorganic layers. As n approaches infinity, the formula describes 3D $MAPbI_3$. (b) Optical microscope image of a Au-coated single crystal of n = 6 ($BA_2MA_5Pb_6I_{19}$).

lation,[11,20] and pinhole control[21] can increase the material's resilience and lifetime but not significantly enough to make it competitive with more stable alternative PV and OE materials such as Si- or Ga-based compounds. Prior studies have shown that exposing $MAPbI_3$ to temperatures as modest as 75−85 °C leads to degradation rates significantly faster than that at room temperature.[12,16−18,22] This thermal instability is responsible for the failure to meet international standards for solar cells, which require that they remain stable up to at least 85 °C (IEC 61646).[23] The exceptionally low thermal conductivity of single-crystal $MAPbI_3$, reported to be κ = 0.34−0.50 W/m·K,[24−27] makes proper thermal management a major challenge to its stability and longevity in devices.

Two-dimensional, layered perovskite structures such as Ruddlesden−Popper (RP) phases have been developed in an effort to retain the desirable features of 3D HOIPs, such as solution processability, and catalyze stability and excitonic effects more akin to conventional PV materials.[28−30] In these structures, n layers of perovskite octahedral cages are separated by organic cationic spacers. The $MAPbI_3$-based RP phases, $BA_2MA_{n-1}Pb_nI_{3n+1}$ (BA = butylammonium) (see Figure 1a), exhibit improved stability in moisture- and light-rich environments due to the presence of hydrophobic BA chains and demonstrate PCEs as high as ∼12.5%.[30−32] These RP phases have shown degradation at 80 °C, though at slower rates than $MAPbI_3$.[15] However, their thermal conductivities and the underlying phonon transport mechanisms, which control their ability to dissipate heat, remain unclear. A recent experimental study of multiple lead halide 2D layered perovskites finds that their thermal conductivities are related to the orientation of the organic spacers relative to the inorganic layers.[33] The importance of the inorganic layer thickness and interface density, controlled by n, was not considered since the structures were not derivates of the same perovskite family. Meanwhile, Rasel *et al.* hypothesize that the decreasing thermal conductivity they observe in $(C_nH_{2n+1}NH_3)_2PbI_4$ 2D perovskites with increasing n may result from phonon transport dependency on organic-chain length.[34]

To that end, interest in the thermal conductivity of $BA_2MA_{n-1}Pb_nI_{3n+1}$ RP phases is 2-fold. Practically, the thermal conductivity is important to maintain appropriate temperatures during device operation. Fundamentally, the naturally occurring 2D architecture of these structures allows for the possibility of coherent interlayer phonon transport. In the context of superlattices, this occurs when phonon modes emerge from the secondary periodicity rather than scatter at the structure's associated interfaces and therefore exhibit "wave-like" instead of "particle-like" transport.[35,36] The so-called coherent phonons can have mean free paths greater than the superlattice period, thus enabling higher thermal conductivities than would be expected in a purely particle-like regime. However, such coherent phonon enhancements to thermal conductivity of layered materials can be hindered by imperfect interfaces that destroy periodicity[35,36] and thus have only been observed in a few cases such as in very high-quality epitaxial oxide heterostructures[34] and GaAs/AlAs superlattices.[36]

Secondary periodicity and the resulting coherent phonons have been studied in RP phases,[37−39] and their effect on thermal conductivity has been considered with mixed conclusions.[40,41] A recent transient reflectance study describes longer period oscillations in $(PEA)_2Pb_nI_{3n+1}$ RP phases with increasing n. While they do not consider how this affects phonon speed, they speculate that it will cause thermal conductivity to increase with increasing n.[40] By contrast, through atomic-level simulations, a separate study concluded that the thermal conductivity of a $SrTiO_3$-based RP phase should decrease with increasing n.[41] Clearly, more experimental thermal conductivity data are required to understand the complex phonon physics and thermal transport in RP phases.

Here, we determine the cross-layer thermal conductivity of thin film and single-crystal $BA_2MA_{n-1}Pb_nI_{3n+1}$ RP phases for n = 1−6 using a high-resolution optical pump−probe technique known as frequency-domain thermoreflectance (FDTR).[42] In doing so, we distinguish the relationship between the thermal conductivity of these RP phases and that of $MAPbI_3$ to consider the implications on the thermal performance and longevity of devices that may implement this class of perovskite material. Moreover, we experimentally observe a decrease in thermal conductivity with increasing n in low-n RP phases of similar orientation, suggesting that the contribution of coherent phonons diminishes as the interface density decreases. We reason that this phenomenon, coupled with the other tunable properties of $BA_2MA_{n-1}Pb_nI_{3n+1}$, identifies pathways for functionality in a wide variety of devices.

https://dx.doi.org/10.1021/acsnano.0c03595
ACS Nano XXXX, XXX, XXX−XXX

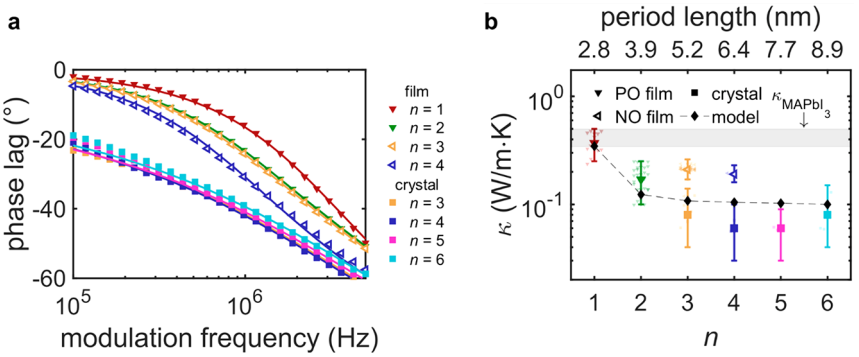

Figure 2. (a) FDTR phase lag data (markers) and fits (lines) for $n = 1-4$ thin films and $n = 3-6$ single crystals. (b) Room-temperature thermal conductivity of $BA_2MA_{n-1}Pb_nI_{3n+1}$ as a function of n for $n = 1-6$. Downward and sideways facing triangles represent thin films that have layers of parallel orientation (PO) and normal orientation (NO) with respect to the substrate, respectively. Squares represent single crystals, and black diamonds represent the predicted thermal conductivity by a reduced-order lattice dynamics model. Semitransparent data are individual measurements, and opaque data are medians of all measurements for the respective sample, where error bars represent the 90th and 10th quantiles of fit distributions generated using a Monte Carlo estimation of uncertainty. The gray-shaded region indicates the range of thermal conductivities reported in the literature for $MAPbI_3$. Period length of the respective structure is labeled on the top axis.

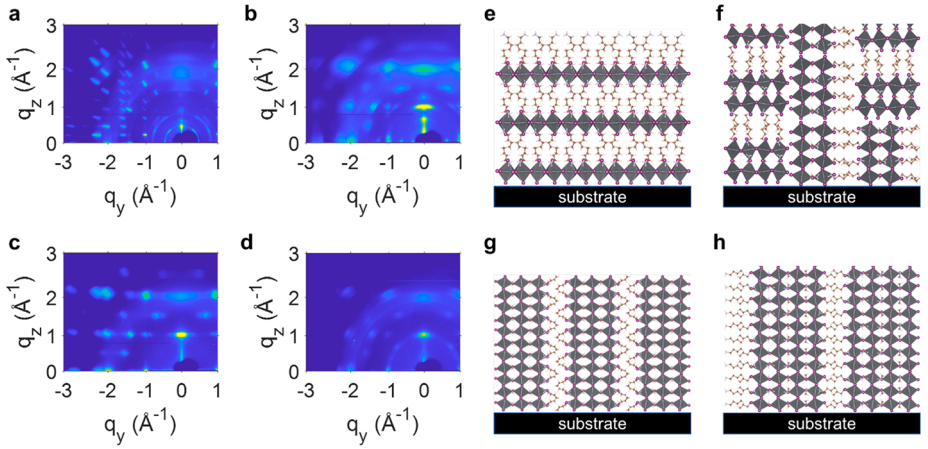

Figure 3. GIWAXS measurements (a–d) and structural interpretation (e–h) of $n = 1-4$ thin films. The [0 1 0] crystal direction of $n = 1$ is oriented normal to the substrate, while this same direction in $n = 3$ and $n = 4$ thin films is loosely parallel to the substrate. $n = 2$ appears to be bimodal, possessing a 2:1 ratio of grains with the [0 1 0] crystal direction oriented normal and parallel to the substrate.

RESULTS AND DISCUSSION

We examine thin films of $n = 1-4$ (thickness range of 40–240 nm) and single crystals of $n = 3-6$ (size range of 0.5–2 mm) (see Figure 1b). Single crystals of $n = 1, 2$ could not be repeatably measured due to their typically smaller size (less than 200 μm), irregular shape, and rough surface topography. We measure thermal conductivity across numerous samples of both single crystals and thin films using FDTR. FDTR periodically heats the sample and monitors the phase lag of surface temperature to heat flux, which is fit using an analytical solution to the heat diffusion equation to extract the sample's unknown thermal conductivity (see Methods for details on sample preparation and FDTR). Fits based solely on thermal conductivities (κ) of RP phases, shown as solid lines in Figure 2a, consistently match the experimental phase lag data over a wide range of frequencies and support the accuracy of this approach.

The thermal conductivities (κ) of $BA_2MA_{n-1}Pb_nI_{3n+1}$ RP phases are shown as a function of n for $n = 1-4$ thin films and $n = 3-6$ single crystals in Figure 2b. Individual measurements are shown as semitransparent markers, whereas the central tendency, represented by the median, for each n is shown as an opaque marker. Upper and lower error bars represent the 90th and 10th quantiles of the distribution of fits generated by a Monte Carlo estimation method, which is used to assess the uncertainty in κ from measurement variability and propagated uncertainty from fitting parameters (see SI Section 2.5).[43,44] The κ values of the thin film RP phases of $n = 1-4$ are ultralow at $0.37 \pm 0.13/0.12$, $0.17 \pm 0.08/0.07$, $0.21 \pm 0.05/0.04$, and $0.19 \pm 0.04/0.03$ W/m·K, and that of the single-crystal RP phases of $n = 3-6$ are even lower at $0.08 \pm 0.06/0.04$, $0.06 \pm 0.04/0.03$, $0.06 \pm 0.03/0.03$, and $0.08 \pm 0.07/0.04$ W/m·K. The κ values of the thin film RP phases initially decrease as n increases, consistent with increased coherent phonon contributions to thermal conductivity in lower n phases. The κ values of $n = 3-6$ single-crystal phases are among the lowest reported for fully dense solids.[45] Additionally, we note that κ values of thin films are larger than that of single crystals for $n = 3, 4$, contrary to the expectation of lower κ due to phonon boundary scattering in thin films.

To discern the origins of the discrepancy between thin films and single crystals, we perform grazing-incidence wide-angle X-ray scattering (GIWAXS) to assess the compositional purity and orientational control of thin film samples of $n = 1-4$. As a hybrid of wide-angle scattering and grazing incidence diffraction, in GIWAXS an X-ray beam is directed at an angle near that of total external reflection with respect to the film surface. Lengths on

https://dx.doi.org/10.1021/acsnano.0c03595
ACS Nano XXXX, XXX, XXX–XXX

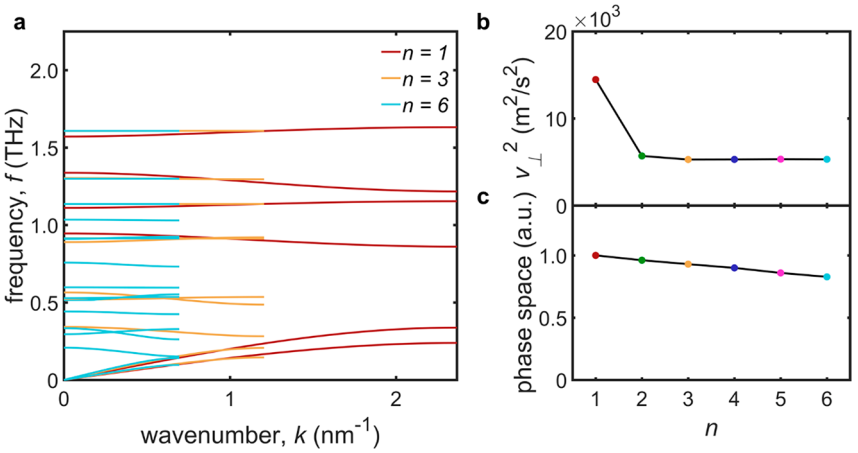

Figure 4. (a) Phonon dispersion relationship of n = 1, 3, and 6 RP phases in the cross-layer [0 1 0] direction. (b) Average cross-layer group velocity of n = 1−6 RP phases. (c) Total phase space, normalized to that of n = 1, of n = 1−6 RP phases.

the order of tens of angstroms, corresponding to the d-spacing in solid-state materials, can be accessed because of the close distance between the detector and the sample. Additionally, the use of a 2D detector allows for the determination of the orientation of diffraction planes in the sample relative to the substrate based on the position along the angular axis χ in which the peak appears.[15,46]

GIWAXS data are shown in Figure 3a for n = 1−4. The peaks present in the measurement for n = 1 indicate a high level of orientational consistency with layers oriented parallel to the substrate as shown in Figure 3e. This result confirms our observation of ultralow cross-layer thermal conductivity ($\kappa_\perp$) in this RP phase, since FDTR measurements primarily probe thermal transport properties normal to the substrate surface. Interestingly, small peaks at low q indicate that there are some impurities in n = 1 samples, possibly resulting from solvated phases created during film formation.[47,48] Data for n = 2, shown in Figure 3b, appear bimodal, with the layers oriented normal and parallel to the substrate surface, with the normal orientation being about twice as common as depicted in Figure 3f. This ratio is determined through calculation of the area under the (1 11 1) peak for each orientation (see SI Section 3.2). Data for n = 3, 4 shown in Figure 3c and d have layers oriented normal to the substrate depicted in Figure 3g and h. Notably, the n = 4 member has peaks that have been broadened along χ, the angular axis, which indicates that the layers deviate by a couple of degrees from perfectly normal. In this orientation, heat will flow along the layers for n = 3, 4. We expect that the in-layer κ of RP phases will more closely resemble that of bulk $MAPbI_3$ (κ = 0.34−0.50 W/m·K) as phonons travel along the inorganic lead iodide layers. Hence, higher measured values of thermal conductivity for n = 3, 4 thin films, relative to single crystals, are not a true reflection of $\kappa_\perp$, but are rather a consequence of the films' grain orientations.

In addition to GIWAXS, we characterize the composition and orientation of structures in n = 1−4 RP thin films using powder X-ray diffraction, or PXRD (see SI Section 4). We find that peaks in the n = 1 measurement correspond to planes parallel to the substrate and that there are no features consistent with other orientations. Our measurement of n = 2 corroborates the bimodal distribution of orientations observed in the GIWAXS measurement, with peaks being associated with planes both perpendicular and parallel to the substrate. The major peak found in the measurements of n = 3, 4 thin films corresponds to the (2 0 2) plane, and the minor peak is associated with the (1 1 1) plane that lies at an angle with respect to the substrate. Given that the former peak is significantly stronger than the latter, we conclude that the majority of the structure is oriented perpendicular to the substrate in both films.

While our measurements are consistent with the value reported by Giri *et al.* for the n = 4 thin film with similar orientation (0.19 ± 0.04/0.03 W/m·K *vs* 0.17 ± 0.03 W/m·K),[33] we find lower values of $\kappa_\perp$ in n = 4 single crystals due to transport being exclusively cross-layer. We measure a comparatively higher $\kappa_\perp$ in n = 1, or $(CH_3NH_3)_2PbI_4$, thin films than that reported by both Giri *et al.* for thin films (0.18 ± 0.04 W/m·K) and Rasel *et al.* for single crystals (0.125 ± 0.089 W/m·K).[34] Notably, the steady-state temperature rise in samples of n = 1 resulting from our laser heating (14.6 K, see SI Section 2.6) is similar to that of Giri *et al.* (14 K) and is lower than that of Rasel *et al.* (30 K). It is possible that the lower thermal conductivity reported by Rasel *et al.* may arise from laser heating induced structural rearrangements that they hypothesize exist at and beyond ∼325 K based on their heat capacity data. Such structural rearrangements could hinder phonon transport and therefore reduce apparent thermal conductivity. By comparison, the difference between our reported value and that of Giri *et al.* may originate from variation in film preparation, particularly the use of different solvents and substrate temperatures during deposition, which are well known to affect film morphology, homogeneity, and composition.[31,48−50]

The overarching trend in Figure 2b is that $\kappa_\perp$ (filled opaque data in Figure 2b; n = 1, 2 thin films and n = 3−6 single crystals) of the RP phases initially decreases as n and the interface spacing increases and levels off at higher n. Generally, our findings suggest that thermal conductivity is possibly related to layer spacing by way of coherent phonon transport. In any superlattice there will be a coexistence of emergent coherent phonons that transmit through interfaces, and incoherent phonons that maintain the character of one constituent layer and scatter at the interfaces. The particle description of phonons suggests that increased interface spacing enables longer phonon mean free paths and therefore higher thermal conductivity. Since we observe the opposite trend, it appears that coherent phonons may contribute significantly to the thermal conductivity of n = 1, 2 RP phases. We hypothesize that phonon coherence plays a less significant role in the thermal conductivities of n = 3−6 phases given their relative insensitivity to n.

https://dx.doi.org/10.1021/acsnano.0c03595
ACS Nano XXXX, XXX, XXX−XXX

The cross-layer thermal conductivity can be expressed as

$$\kappa_{\perp} = \sum_{\beta} C_{\beta} v_{\perp,\beta}^2 \tau_{\beta} \quad (1)$$

where β indexes the phonon mode and C, $v_{\perp}$, and τ represent the modal heat capacity, cross-layer component of group velocity, and relaxation time. To quantitatively understand the effect of coherent phonon group velocity on $\kappa_{\perp}$ in $BA_2MA_{n-1}Pb_nI_{3n+1}$, we perform a reduced-order harmonic lattice dynamics calculation. To limit computational cost and modeling complexity,[51] we group atoms together to form octahedron-like and BA-like beads (see SI Section 5.1) that interact harmonically according to the equations of motion. Three spring constants are invoked to generate the equations of motion in this system: octahedron−octahedron, BA−BA, and BA−octahedron. The first is fit from the experimental dispersion of $MAPbI_3$,[52] whereas the other two are derived from experimentally determined sound speeds.[53] These equations of motion are used in an assumed plane wave solution to determine the coherent phonon dispersion relations.[54−57] With BA omitted, the model accurately reproduces the acoustic phonon dispersion of $MAPbI_3$ (see SI Section 5.3).[52] By using a reduced-order model, we ignore high-frequency incoherent phonon modes due to the localized internal vibrations of the $MAPbI_3$ or BA molecules.

The nonintuitive trend in $\kappa_{\perp}$ with n can be explained by the lattice dynamics that capture the effects of emergent coherent phonons. In Figure 4a we show the phonon dispersion relationships for n = 1, 3, and 6 in the cross-layer [0 1 0] direction. As n increases there is more band flattening at high wavevectors and an increased number of phonon bandgaps resulting from the increased bead number density. Generally, this band flattening reduces the cross-layer coherent phonon group velocities and is especially pronounced between n = 1 and n = 2. The Brillouin zone averaged $v_{\perp}^2$ decreases by more than 60% from n = 1 to n = 2, then decreases more gradually with increasing n, as shown in Figure 4b. Phonon scattering trends with n may, however, produce a competing effect on thermal conductivity. The fraction of the phonon frequency range occupied by bandgaps increases with increasing n, which reduces the phase space for scattering of coherent phonons (*i.e.*, the number of possible three-phonon scattering events that conserve energy and momentum) as shown in Figure 4c. Reduced phonon phase space typically causes increased relaxation times and thus increased thermal conductivity, but the gradual reduction in phase space with n may be offset by reduced $v_{\perp}^2$ and an 8% reduction in C_{β} (see SI Section 5.4) to create a flat $\kappa_{\perp}$ trend for n = 3−6.

Our harmonic model cannot be used to directly predict $\kappa_{\perp}$ since the average phonon lifetime $\bar{\tau}_n$ for n = 1−6 is not modeled. However, the correspondence of $\kappa_{\perp}$ data to the average $v_{\perp}^2$ and the relative invariance of phase space led us to fit eq 1 to the $\kappa_{\perp}$ data by choosing a single $\bar{\tau}$ across all n that minimizes the mean square error. We find a $\bar{\tau}$ for coherent phonons across n = 1−6 RP phases of ∼100 ps, resulting in a predicted thermal conductivity that agrees well with experimental data across all n (excluding films with n = 3, 4), as shown in Figure 2b. While phonon relaxation times typically span orders of magnitude, the close fit of $\kappa_{\perp}$ among all n to a single $\bar{\tau}$ suggests that those of coherent phonons that may contribute heavily to $\kappa_{\perp}$ have a narrower distribution. An average relaxation time of 100 ps corresponds to average cross-layer mean free paths ($\bar{\Lambda}_{\perp} = \bar{\tau}\sqrt{\overline{v_{\perp}^2}}$) of coherent phonons spanning 7 nm for n = 6 to 12 nm for n = 1, which are larger than or similar to the period length.

CONCLUSIONS

In summary, we determine thermal conductivity perpendicular to the layers, $\kappa_{\perp}$, of $BA_2MA_{n-1}Pb_nI_{3n+1}$ RP phases using FDTR and find that it decreases with increasing n, particularly at low n. We predict that the observed trend in $\kappa_{\perp}$ is due to a reduction in coherent phonon transport in higher n RP phases. According to our measurements, single crystals of n = 3−6 all present ultralow thermal conductivities on the order of the lowest ever observed in fully dense solids. Our coarse-grain 3D lattice dynamics calculations reveal that the average of the square of cross-layer sound velocity, $\overline{v_{\perp}^2}$, of coherent phonons decreases with n at a rate consistent with our experimental $\kappa_{\perp}$ data. Our findings suggest that while these RP phases are more stable than $MAPbI_3$ at elevated temperatures, their ultralow $\kappa_{\perp}$ may make maintaining serviceably low temperatures challenging. However, varying n allows for tunability in thermal conductivity and other material properties, which unlocks a myriad of possibilities for design in PV, OE, and thermal transport applications.

METHODS

Sample Preparation. Thin film RP phases with thicknesses of 40−240 nm are spin coated onto Si substrates. Single crystals, typically 0.5−2.0 mm in major dimension (as shown in Figure 1b), are precipitated from aqueous solution and epoxied to SiO_2 substates. Single crystals are exfoliated using Kapton tape to expose a pristine layer of material. Thin films and single crystals are then sputtered or evaporated with 60−110 nm of Au. Profilometry is used to determine the thickness of the deposited Au layer, as well as that of the underlying perovskite layer in the case of the thin films. Samples are kept in a dark Ar glovebox environment except for transport, metal deposition, and measurement to minimize the possibility of contamination or exposure.

FDTR. In FDTR, the sample is heated by a 488 nm continuous-wave (CW) pump laser that is intensity-modulated over frequencies ranging from 100 kHz to 5 MHz. Periodic heating generates a periodic change in the sample's surface temperature, with a phase lag that depends on the thermal conductivity of the RP phase sample. Thermoreflectance of the Au coating causes modulation of a reflected 532 nm CW probe laser, and its phase lag relative to the pump is monitored by a lock-in amplifier. The phase lag of the probe to pump (temperature to heating) is fit to a solution of the heat diffusion equation for a periodically heated layered structure to determine the unknown RP phase thermal conductivity, as shown in Figure 2a.[58]

The analytical solution used to fit the FDTR data relies on thermophysical properties of the sample such as its thickness and specific heat. The RP phases' volumetric heat capacities are not directly measured, so they are estimated based on the molar heat capacities of the structure's three constituent materials (BA, $MAPbI_3$, and PbI_4) and the volume of the unit cell. In the case of the thin films, the fit solution is insensitive to this parameter within the range of our measurements (see SI Section 2.4), so imprecision in this approximation does not significantly impact the quality of fit, quantified as a mean-squared error.

GIWAXS. GIWAXS is performed at Beamline 12-ID-B of the Advanced Photon Source at Argonne National Laboratory. A PerkinElmer XRpad (PerkinElmer Inc.) detector is employed with the sample-to-detector distance set to 18 cm. The energy of X-ray radiation is 13.3 keV. The samples used in GIWAXS measurements are deposited on silicon wafer substrates. The substrates are first aligned to be parallel to the X-ray beam, and the GIWAXS data are collected at an X-ray beam incidence angle of ∼0.1°. Curves are fit to the data using the LineFit toolbox, while plots are generated using the GIXSGUI program.[59] Simulations of $MAPbI_3$ and BA at different orientations are created by LeeTool, a MATLAB-software package written by

https://dx.doi.org/10.1021/acsnano.0c03595
ACS Nano XXXX, XXX, XXX−XXX

Byeongdu Lee, available at the 12-ID-B beamline of the Advanced Photon Source (APS) at Argonne National Lab.

ASSOCIATED CONTENT

Supporting Information

The Supporting Information is available free of charge at https://pubs.acs.org/doi/10.1021/acsnano.0c03595.

Sample preparation and characterization, frequency-domain thermoreflectance model parameters, sensitivity, uncertainty, heating analysis, GIWAXS and PXRD acquisition and analysis, lattice dynamics model framework (PDF)

AUTHOR INFORMATION

Corresponding Authors

Alexander D. Christodoulides − *Department of Mechanical Engineering, Carnegie Mellon University, Pittsburgh, Pennsylvania 15213, United States*; Email: achristo@andrew.cmu.edu

Jonathan A. Malen − *Department of Mechanical Engineering, Carnegie Mellon University, Pittsburgh, Pennsylvania 15213, United States; Department of Materials Science, Carnegie Mellon University, Pittsburgh, Pennsylvania 15213, United States;* orcid.org/0000-0003-4560-4476; Email: jonmalen@andrew.cmu.edu

Authors

Peijun Guo − *Center for Nanoscale Materials, Argonne National Laboratory, Lemont, Illinois 60439, United States; Department of Chemical and Environmental Engineering, Yale University, New Haven, Connecticut 06520, United States;* orcid.org/0000-0001-5732-7061

Lingyun Dai − *Department of Mechanical Engineering, Carnegie Mellon University, Pittsburgh, Pennsylvania 15213, United States*

Justin M. Hoffman − *Department of Chemistry, Northwestern University, Evanston, Illinois 60208, United States*

Xiaotong Li − *Department of Chemistry, Northwestern University, Evanston, Illinois 60208, United States;* orcid.org/0000-0001-7107-7273

Xiaobing Zuo − *X-ray Sciences Division, Argonne National Laboratory, Lemont, Illinois 60439, United States*

Daniel Rosenmann − *Center for Nanoscale Materials, Argonne National Laboratory, Lemont, Illinois 60439, United States*

Alexandra Brumberg − *Department of Chemistry, Northwestern University, Evanston, Illinois 60208, United States;* orcid.org/0000-0003-2512-4686

Mercouri G. Kanatzidis − *Department of Chemistry, Northwestern University, Evanston, Illinois 60208, United States;* orcid.org/0000-0003-2037-4168

Richard D. Schaller − *Center for Nanoscale Materials, Argonne National Laboratory, Lemont, Illinois 60439, United States; Department of Chemistry, Northwestern University, Evanston, Illinois 60208, United States;* orcid.org/0000-0001-9696-8830

Complete contact information is available at: https://pubs.acs.org/10.1021/acsnano.0c03595

Notes

The authors declare no competing financial interest.

ACKNOWLEDGMENTS

A.D.C., L.D., and J.A.M. acknowledge support from the Army Research Office, Grant No. W911NF-17-1-0397, as well as support from the Wilton E. Scott Institute for Energy Innovation. A.B. acknowledges support from the National Science Foundation Graduate Research Fellowship Program under Grant No. DGE-1324585. M.G.K., A.B., and X.L. acknowledge support from the Office of Naval Research (ONR) under Grant N00014-20-1-2725. This work was performed, in part, at the Center for Nanoscale Materials using resources of the Advanced Photon Source, a U.S. Department of Energy Office of Science User Facility, and supported by the U.S. Department of Energy, Office of Science, under Contract No. DE-AC02-06CH11357.

REFERENCES

(1) Brenner, T. M.; Egger, D. A.; Kronik, L.; Hodes, G.; Cahen, D. Hybrid Organic-Inorganic Perovskites: Low-Cost Semiconductors with Intriguing Charge-Transport Properties. *Nat. Rev. Mater.* **2016**, *1*, 15007.

(2) Leguy, A. M. A.; Azarhoosh, P.; Alonso, M. I.; Campoy-Quiles, M.; Weber, O. J.; Yao, J.; Bryant, D.; Weller, M. T.; Nelson, J.; Walsh, A.; Van Schilfgaarde, M.; Barnes, P. R. F. Experimental and Theoretical Optical Properties of Methylammonium Lead Halide Perovskites. *Nanoscale* **2016**, *8* (12), 6317−6327.

(3) Stranks, S. D.; Snaith, H. J. Metal-Halide Perovskites for Photovoltaic and Light-Emitting Devices. *Nat. Nanotechnol.* **2015**, *10*, 391−402.

(4) Veldhuis, S. A.; Boix, P. P.; Yantara, N.; Li, M.; Sum, T. C.; Mathews, N.; Mhaisalkar, S. G. Perovskite Materials for Light-Emitting Diodes and Lasers. *Adv. Mater.* **2016**, *28* (32), 6804−6834.

(5) Raghavan, C. M.; Chen, T. P.; Li, S. S.; Chen, W. L.; Lo, C. Y.; Liao, Y. M.; Haider, G.; Lin, C. C.; Chen, C. C.; Sankar, R.; Chang, Y. M.; Chou, F. C.; Chen, C. W. Low-Threshold Lasing from 2D Homologous Organic-Inorganic Hybrid Ruddlesden-Popper Perovskite Single Crystals. *Nano Lett.* **2018**, *18* (5), 3221−3228.

(6) Du, M. H. Efficient Carrier Transport in Halide Perovskites: Theoretical Perspectives. *J. Mater. Chem. A* **2014**, *2* (24), 9091−9098.

(7) Burschka, J.; Pellet, N.; Moon, S. J.; Humphry-Baker, R.; Gao, P.; Nazeeruddin, M. K.; Grätzel, M. Sequential Deposition as a Route to High-Performance Perovskite-Sensitized Solar Cells. *Nature* **2013**, *499* (7458), 316−319.

(8) Miyata, K.; Meggiolaro, D.; Tuan Trinh, M.; Joshi, P. P.; Mosconi, E.; Jones, S. C.; De Angelis, F.; Zhu, X. Y. Large Polarons in Lead Halide Perovskites. *Sci. Adv.* **2017**, *3* (8), 1701217.

(9) Herz, L. M. Charge-Carrier Dynamics in Organic-Inorganic Metal Halide Perovskites. *Annu. Rev. Phys. Chem.* **2016**, *67* (1), 65−89.

(10) Milot, R. L.; Sutton, R. J.; Eperon, G. E.; Haghighirad, A. A.; Martinez Hardigree, J.; Miranda, L.; Snaith, H. J.; Johnston, M. B.; Herz, L. M. Charge-Carrier Dynamics in 2D Hybrid Metal-Halide Perovskites. *Nano Lett.* **2016**, *16* (11), 7001−7007.

(11) Kim, H.; Lee, J.; Kim, B.; Byun, H. R.; Kim, S. H.; Oh, H. M.; Baik, S.; Jeong, M. S. Enhanced Stability of $MAPbI_3$ Perovskite Solar Cells Using Poly(*p*-Chloro-Xylylene) Encapsulation. *Sci. Rep.* **2019**, *9* (1), 1−6.

(12) Wang, S.; Jiang, Y.; Juarez-Perez, E. J.; Ono, L. K.; Qi, Y. Accelerated Degradation of Methylammonium Lead Iodide Perovskites Induced by Exposure to Iodine Vapour. *Nat. Energy* **2017**, *2* (1), 1−8.

(13) Berhe, T. A.; Su, W. N.; Chen, C. H.; Pan, C. J.; Cheng, J. H.; Chen, H. M.; Tsai, M. C.; Chen, L. Y.; Dubale, A. A.; Hwang, B. J. Organometal Halide Perovskite Solar Cells: Degradation and Stability. *Energy Environ. Sci.* **2016**, *9*, 323−356.

(14) Alberti, A.; Deretzis, I.; Pellegrino, G.; Bongiorno, C.; Smecca, E.; Mannino, G.; Giannazzo, F.; Condorelli, G. G.; Sakai, N.; Miyasaka, T.; Spinella, C.; La Magna, A. Similar Structural Dynamics for the Degradation of $CH_3NH_3PbI_3$ in Air and in Vacuum. *ChemPhysChem* **2015**, *16* (14), 3064−3071.

(15) Tsai, H.; Nie, W.; Blancon, J. C.; Stoumpos, C. C.; Asadpour, R.; Harutyunyan, B.; Neukirch, A. J.; Verduzco, R.; Crochet, J. J.; Tretiak, S.; Pedesseau, L.; Even, J.; Alam, M. A.; Gupta, G.; Lou, J.; Ajayan, P. M.; Bedzyk, M. J.; Kanatzidis, M. G.; Mohite, A. D. High-Efficiency Two-Dimensional Ruddlesden-Popper Perovskite Solar Cells. *Nature* **2016**, *536* (7616), 312−317.

(16) Han, Y.; Meyer, S.; Dkhissi, Y.; Weber, K.; Pringle, J. M.; Bach, U.; Spiccia, L.; Cheng, Y. B. Degradation Observations of Encapsulated Planar $CH_3NH_3PbI_3$ Perovskite Solar Cells at High Temperatures and Humidity. *J. Mater. Chem. A* **2015**, *3* (15), 8139−8147.

(17) Abdelmageed, G.; Mackeen, C.; Hellier, K.; Jewell, L.; Seymour, L.; Tingwald, M.; Bridges, F.; Zhang, J. Z.; Carter, S. Effect of Temperature on Light Induced Degradation in Methylammonium Lead Iodide Perovskite Thin Films and Solar Cells. *Sol. Energy Mater. Sol. Cells* **2018**, *174*, 566−571.

(18) Conings, B.; Drijkoningen, J.; Gauquelin, N.; Babayigit, A.; D'Haen, J.; D'Olieslaeger, L.; Ethirajan, A.; Verbeeck, J.; Manca, J.; Mosconi, E.; Angelis, F. De; Boyen, H.-G. Intrinsic Thermal Instability of Methylammonium Lead Trihalide Perovskite. *Adv. Energy Mater.* **2015**, *5* (15), 1500477.

(19) Wu, C.; Li, H.; Yan, Y.; Chi, B.; Felice, K. M.; Moore, R. B.; Magill, B. A.; Mudiyanselage, R. R. H. H.; Khodaparast, G. A.; Sanghadasa, M.; Priya, S. Highly-Stable Organo-Lead Halide Perovskites Synthesized through Green Self-Assembly Process. *Sol. RRL* **2018**, *2* (6), 1800052.

(20) Brinkmann, K. O.; Zhao, J.; Pourdavoud, N.; Becker, T.; Hu, T.; Olthof, S.; Meerholz, K.; Hoffmann, L.; Gahlmann, T.; Heiderhoff, R.; Oszajca, M. F.; Luechinger, N. A.; Rogalla, D.; Chen, Y.; Cheng, B.; Riedl, T. Suppressed Decomposition of Organometal Halide Perovskites by Impermeable Electron-Extraction Layers in Inverted Solar Cells. *Nat. Commun.* **2017**, *8* (1), 1−9.

(21) Ono, L. K.; Raga, S. R.; Remeika, M.; Winchester, A. J.; Gabe, A.; Qi, Y. Pinhole-Free Hole Transport Layers Significantly Improve the Stability of MAPbI3-Based Perovskite Solar Cells under Operating Conditions. *J. Mater. Chem. A* **2015**, *3* (30), 15451−15456.

(22) Kim, N. K.; Min, Y. H.; Noh, S.; Cho, E.; Jeong, G.; Joo, M.; Ahn, S. W.; Lee, J. S.; Kim, S.; Ihm, K.; Ahn, H.; Kang, Y.; Lee, H. S.; Kim, D. Investigation of Thermally Induced Degradation in $CH_3NH_3PbI_3$ Perovskite Solar Cells Using *in Situ* Synchrotron Radiation Analysis. *Sci. Rep.* **2017**, *7* (1), 1−9.

(23) *Testing and Measuring Equipment/Allowed Subcontracting Thin-Film Terrestrial Photovoltaic (PV) Modules-Design Qualification and Type Approval*, 1st ed.; Committee of Testing Laboratories, Eds.; International Electrotechnical Commission: Geneva, 1998.

(24) Elbaz, G. A.; Ong, W.-L.; Doud, E. A.; Kim, P.; Paley, D. W.; Roy, X.; Malen, J. A. Phonon Speed, Not Scattering, Differentiates Thermal Transport in Lead Halide Perovskites. *Nano Lett.* **2017**, *17* (9), 5734−5739.

(25) Ye, T.; Wang, X.; Li, X.; Yan, A. Q.; Ramakrishna, S.; Xu, J. Ultra-High Seebeck Coefficient and Low Thermal Conductivity of a Centimeter-Sized Perovskite Single Crystal Acquired by a Modified Fast Growth Method. *J. Mater. Chem. C* **2017**, *5* (5), 1255−1260.

(26) Pisoni, A.; Jaćimović, J.; Barišić, O. S.; Spina, M.; Gaál, R.; Forró, L.; Horváth, E. Ultra-Low Thermal Conductivity in Organic−Inorganic Hybrid Perovskite $CH_3NH_3PbI_3$. *J. Phys. Chem. Lett.* **2014**, *5* (14), 2488−2492.

(27) Heiderhoff, R.; Haeger, T.; Pourdavoud, N.; Hu, T.; Al-Khafaji, M.; Mayer, A.; Chen, Y.; Scheer, H. C.; Riedl, T. Thermal Conductivity of Methylammonium Lead Halide Perovskite Single Crystals and Thin Films: A Comparative Study. *J. Phys. Chem. C* **2017**, *121* (51), 28306−28311.

(28) Smith, I. C.; Hoke, E. T.; Solis-Ibarra, D.; McGehee, M. D.; Karunadasa, H. I. A Layered Hybrid Perovskite Solar-Cell Absorber with Enhanced Moisture Stability. *Angew. Chem.* **2014**, *126* (42), 11414−11417.

(29) Myae Soe, C. M.; Nagabhushana, G. P.; Shivaramaiah, R.; Tsai, H.; Nie, W.; Blancon, J. C.; Melkonyan, F.; Cao, D. H.; Traoré, B.; Pedesseau, L.; Kepenekian, M.; Katan, C.; Even, J.; Marks, T. J.; Navrotsky, A.; Mohite, A. D.; Stoumpos, C. C.; Kanatzidis, M. G. Structural and Thermodynamic Limits of Layer Thickness in 2D Halide Perovskites. *Proc. Natl. Acad. Sci. U. S. A.* **2019**, *116* (1), 58−66.

(30) Cao, D. H.; Stoumpos, C. C.; Farha, O. K.; Hupp, J. T.; Kanatzidis, M. G. 2D Homologous Perovskites as Light-Absorbing Materials for Solar Cell Applications. *J. Am. Chem. Soc.* **2015**, *137* (24), 7843−7850.

(31) Stoumpos, C. C.; Cao, D. H.; Clark, D. J.; Young, J.; Rondinelli, J. M.; Jang, J. I.; Hupp, J. T.; Kanatzidis, M. G. Ruddlesden-Popper Hybrid Lead Iodide Perovskite 2D Homologous Semiconductors. *Chem. Mater.* **2016**, *28* (8), 2852−2867.

(32) Mao, L.; Kennard, R. M.; Traore, B.; Ke, W.; Katan, C.; Even, J.; Chabinyc, M. L.; Stoumpos, C. C.; Kanatzidis, M. G. Seven-Layered 2D Hybrid Lead Iodide Perovskites. *Chem.* **2019**, *5* (10), 2593−2604.

(33) Giri, A.; Chen, A. Z.; Mattoni, A.; Aryana, K.; Zhang, D.; Hu, X.; Lee, S.-H.; Choi, J. J.; Hopkins, P. E. Ultralow Thermal Conductivity of Two-Dimensional Metal Halide Perovskites. *Nano Lett.* **2020**, *20* (5), 3331−3337.

(34) Rasel, M. A. J.; Giri, A.; Olson, D. H.; Ni, C.; Hopkins, P. E.; Feser, J. P. Chain-Length Dependence of Thermal Conductivity in 2D Alkylammonium Lead Iodide Single Crystals. *ACS Appl. Mater. Interfaces* **2020**, *12*, 53705−53711.

(35) Ravichandran, J.; Yadav, A. K.; Cheaito, R.; Rossen, P. B.; Soukiassian, A.; Suresha, S. J.; Duda, J. C.; Foley, B. M.; Lee, C. H.; Zhu, Y.; Lichtenberger, A. W.; Moore, J. E.; Muller, D. A.; Schlom, D. G.; Hopkins, P. E.; Majumdar, A.; Ramesh, R.; Zurbuchen, M. A. Crossover from Incoherent to Coherent Phonon Scattering in Epitaxial Oxide Superlattices. *Nat. Mater.* **2014**, *13* (2), 168−172.

(36) Luckyanova, M. N.; Garg, J.; Esfarjani, K.; Jandl, A.; Bulsara, M. T.; Schmidt, A. J.; Minnich, A. J.; Chen, S.; Dresselhaus, M. S.; Ren, Z.; Fitzgerald, E. A.; Chen, G. Coherent Phonon Heat Conduction in Superlattices. *Science (Washington, DC, U. S.)* **2012**, *338* (6109), 936−939.

(37) Mauck, C. M.; France-Lanord, A.; Hernandez Oendra, A. C.; Dahod, N. S.; Grossman, J. C.; Tisdale, W. A. Inorganic Cage Motion Dominates Excited-State Dynamics in 2D-Layered Perovskites $(C_xH_{2x+1}NH_3)_2PbI_4$ (x = 4−9). *J. Phys. Chem. C* **2019**, *123* (45), 27904−27916.

(38) Thouin, F.; Valverde-Chávez, D. A.; Quarti, C.; Cortecchia, D.; Bargigia, I.; Beljonne, D.; Petrozza, A.; Silva, C.; Srimath Kandada, A. R. Phonon Coherences Reveal the Polaronic Character of Excitons in Two-Dimensional Lead Halide Perovskites. *Nat. Mater.* **2019**, *18* (4), 349−356.

(39) Guo, Z.; Wu, X.; Zhu, T.; Zhu, X.; Huang, L. Electron-Phonon Scattering in Atomically Thin 2D Perovskites. *ACS Nano* **2016**, *10* (11), 9992−9998.

(40) Maity, P.; Yin, J.; Cheng, B.; He, J.-H.; Bakr, O. M.; Mohammed, O. F.; Arabia, S. Layer-Dependent Coherent Acoustic Phonons in Two-Dimensional Ruddlesden−Popper Perovskite Crystals. *J. Phys. Chem. Lett.* **2019**, *10*, 5259−5264.

(41) Chernatynskiy, A.; Grimes, R. W.; Zurbuchen, M. A.; Clarke, D. R.; Phillpot, S. R. Crossover in Thermal Transport Properties of Natural, Perovskite-Structured Superlattices. *Appl. Phys. Lett.* **2009**, *95* (16), 161906.

(42) Regner, K. T.; Majumdar, S.; Malen, J. A. Instrumentation of Broadband Frequency Domain Thermoreflectance for Measuring Thermal Conductivity Accumulation Functions. *Rev. Sci. Instrum.* **2013**, *84* (6), 064901.

(43) Bougher, T. L.; Yates, L.; Lo, C. F.; Johnson, W.; Graham, S.; Cola, B. A. Thermal Boundary Resistance in GaN Films Measured by Time Domain Thermoreflectance with Robust Monte Carlo Uncertainty Estimation. *Nanoscale Microscale Thermophys. Eng.* **2016**, *20* (1), 22−32.

(44) Saha, D.; Yu, X.; Du, Y.; Guo, Z.; Xiong, F.; Gellman, A.; Malen, J. Enhancing Thermal Interface Conductance to Graphene Using Ni−Pd Alloy Contacts. *ACS Appl. Mater. Interfaces* **2020**, *12*, 59.

(45) Chiritescu, C.; Cahill, D. G.; Nguyen, N.; Johnson, D.; Bodapati, A.; Keblinski, P.; Zschack, P. Ultralow Thermal Conductivity in Disordered, Layered WSe_2 Crystals. *Science (Washington, DC, U. S.)* **2007**, *315* (5810), 351−353.

https://dx.doi.org/10.1021/acsnano.0c03595
ACS Nano XXXX, XXX, XXX−XXX

(46) Smilgies, D. M. Grazing-Incidence X-Ray Scattering of Lamellar Thin Films. *J. Appl. Crystallogr.* **2019**, *52* (2), 247−251.
(47) Zhang, X.; Munir, R.; Xu, Z.; Liu, Y.; Tsai, H.; Nie, W.; Li, J.; Niu, T.; Smilgies, D. M.; Kanatzidis, M. G.; Mohite, A. D.; Zhao, K.; Amassian, A.; Liu, S. F. Phase Transition Control for High Performance Ruddlesden−Popper Perovskite Solar Cells. *Adv. Mater.* **2018**, *30* (21), 1707166.
(48) Dahlman, C. J.; Decrescent, R. A.; Venkatesan, N. R.; Kennard, R. M.; Wu, G.; Everest, M. A.; Schuller, J. A.; Chabinyc, M. L. Controlling Solvate Intermediate Growth for Phase-Pure Organic Lead Iodide Ruddlesden-Popper $(C_4H_9NH_3)_2(CH_3NH_3)_{n-1}Pb_nI_{3n+1}$ Perovskite Thin Films. *Chem. Mater.* **2019**, *31* (15), 5832−5844.
(49) Qin, Y.; Zhong, H.; Intemann, J. J.; Leng, S.; Cui, M.; Qin, C.; Xiong, M.; Liu, F.; Jen, A. K. -Y.; Yao, K. Coordination Engineering of Single-Crystal Precursor for Phase Control in Ruddlesden−Popper Perovskite Solar Cells. *Adv. Energy Mater.* **2020**, *10* (16), 1904050.
(50) Stoumpos, C. C.; Soe, C. M. M.; Tsai, H.; Nie, W.; Blancon, J. C.; Cao, D. H.; Liu, F.; Traoré, B.; Katan, C.; Even, J.; Mohite, A. D.; Kanatzidis, M. G. High Members of the 2D Ruddlesden-Popper Halide Perovskites: Synthesis, Optical Properties, and Solar Cells of $(CH_3(CH_2)_3NH_3)_2(CH_3NH_3)_4Pb_5I_{16}$. *Chem.* **2017**, *2* (3), 427−440.
(51) Kmiecik, S.; Gront, D.; Kolinski, M.; Wieteska, L.; Dawid, A. E.; Kolinski, A. Coarse-Grained Protein Models and Their Applications. *Chem. Rev.* **2016**, *116* (14), 7898−7936.
(52) Beecher, A. N.; Semonin, O. E.; Skelton, J. M.; Frost, J. M.; Terban, M. W.; Zhai, H.; Alatas, A.; Owen, J. S.; Walsh, A.; Billinge, S. J. L. Direct Observation of Dynamic Symmetry Breaking above Room Temperature in Methylammonium Lead Iodide Perovskite. *ACS Energy Lett.* **2016**, *1* (4), 880−887.
(53) Guo, P.; Stoumpos, C. C.; Mao, L.; Sadasivam, S.; Ketterson, J. B.; Darancet, P.; Kanatzidis, M. G.; Schaller, R. D. Cross-Plane Coherent Acoustic Phonons in Two-Dimensional Organic-Inorganic Hybrid Perovskites. *Nat. Commun.* **2018**, *9* (1), 1−9.
(54) Maris, H.; Tanaka, Y. Phonon Group Velocity and Thermal Conduction in Superlattices. *Phys. Rev. B: Condens. Matter Mater. Phys.* **1999**, *60* (4), 2627−2630.
(55) Yang, B.; Chen, G. Lattice Dynamics Study of Anisotropic Heat Conduction in Superlattices. *Microscale Thermophys. Eng.* **2001**, *5* (2), 107−116.
(56) Kiselev, A. A.; Kim, K. W.; Stroscio, M. A. Thermal Conductivity of Si/Ge Superlattices: A Realistic Model with a Diatomic Unit Cell. *Phys. Rev. B: Condens. Matter Mater. Phys.* **2000**, *62* (11), 6896−6899.
(57) Bies, W. E.; Radtke, R. J.; Ehrenreich, H. Phonon Dispersion Effects and the Thermal Conductivity Reduction in GaAs/AlAs Superlattices. *J. Appl. Phys.* **2000**, *88* (3), 1498−1503.
(58) Cahill, D. G. Analysis of Heat Flow in Layered Structures for Time-Domain Thermoreflectance. *Rev. Sci. Instrum.* **2004**, *75* (12), 5119−5122.
(59) Jiang, Z. GIXSGUI: A MATLAB Toolbox for Grazing-Incidence X-Ray Scattering Data Visualization and Reduction, and Indexing of Buried Three-Dimensional Periodic Nanostructured Films. *J. Appl. Crystallogr.* **2015**, *48* (3), 917−926.

https://dx.doi.org/10.1021/acsnano.0c03595
ACS Nano XXXX, XXX, XXX−XXX